JOURNAL OF AIRCRAFT
Vol. 40, No. 4, July–August 2003

Unsteady Overset Simulation of Rotor-Airframe Interaction

Nathan Hariharan*
United Technologies Research Center, East Hartford, Connecticut 06018
and
Lakshmi N. Sankar†
Georgia Tech, Atlanta, Georgia 30332

Inviscid, three-dimensional, unsteady flow computational results for the aerodynamic interaction between a rotor and a hemispherical-cylinder airframe are presented. A multiblock strategy is used, with separate grids for the fuselage and the rotor blades. An overset grid methodology is used to communicate the flow information between the grids. In each grid a second-order temporally accurate, fifth-order spatially accurate, implicit finite volume scheme is employed to solve the Euler equations. The vortical wake generated by the blade is captured from first principles. The vorticity patterns that impinge on the airframe are analyzed, and the surface-pressure distributions on the airframe are compared with experimental values.

Nomenclature

$|A|$ = Roe's dissipation matrix
C_p = pressure coefficient
$\boldsymbol{e}_x, \boldsymbol{e}_y, \boldsymbol{e}_z$ = unit vectors
$\boldsymbol{F}, \boldsymbol{G}, \boldsymbol{H}$ = flux vector for inviscid fluxes
$\boldsymbol{F}_v, \boldsymbol{G}_v, \boldsymbol{H}_v$ = flux vector for viscous fluxes
$\boldsymbol{M}, \boldsymbol{T}$ = transformation matrices
M_{tip} = tip Mach number (for rotor blade)
M_∞ = freestream Mach number
$\boldsymbol{q}$ = vector of primitive flow variables
$\boldsymbol{q}_L$ = left-hand side flow vector at a given face
$\boldsymbol{q}_R$ = right-hand side flow vector at a given face
R = residual, rotor disk radius
V_F = fluid velocity
V_G = grid velocity
α = angle of attack
ΔS = face surface area
λ = advance ratio
ξ, η, ζ = coordinate directions in the computational plane
τ = time
Ω = rotor angular velocity

Introduction

THE presence of a vortical wake structure beneath the rotor strongly influences the flowfield around the various components of the airframe of the helicopter. In forward flight this wake flow combines with the freestream, creating a complex unsteady flowfield around the airframe. Rotor and airframe components designed without fully taking these interactional effects into account tend to perform below their capabilities and have poor handling qualities. The need to understand the various aspects of rotor-airframe interactional aerodynamics has led to a growth of research activities in this area over the past two decades.

Sheridan and Smith[1] reviewed the interactional problem and classified the categories of interactions. Smith and Betzina[2] studied the interaction between a helicopter rotor and a model fuselage at low speeds. The authors of Refs. 3–7 at Georgia Tech have extensively documented the interactional effects of a rotor with a model airframe through a systematic series of experimental studies. Crouse et al.[8] at the University of Maryland performed similar experiments on an airframe with simulated tail boom. Researchers at NASA Langley Research Center have studied the effects of the airframe on the inflow through the rotor disc.[9]

Most of the initial efforts in modeling rotor-airframe interactions have been with the use of Lagrangean free-wake methods.[8] Researchers like Clark and Maskew,[10] Mavris,[11] and Lorber and Egolf[12] have used variations of this method to simulate the vortical flowfield and to study the interaction with the airframe. Zori et al.[13] and Chaffin and Berry[14] used body forces to account for the presence of the rotor, in solving for the flowfield around an airframe. With rapid advancement of computer speeds, increased memory availability, and improved algorithms, Euler/Navier–Stokes simulation of rotor flowfields including the wake has become feasible.

Examples of such work are the TURNS code simulations by Srinivasan and Baeder[15] and the higher-order simulations of a rotor/wing wake by Hariharan and Sankar[16,17] Navier–Stokes methods have been used in conjunction with overset grids to solve for flowfield around rotor-airframe configurations. Duque and Dimanlig[18] used this approach to study the flowfield around a Comanche helicopter. Meakin[19] used overset grids to simulate the flowfield around the Osprey tilt rotorcraft. Ahmad and Duque[20] have used a similar technique to capture the tip vortices of a rotor in forward flight.

The focus of this research effort is to develop and validate a first-principles-based methodology that can model rotor-airframe interactions. The terminology "first principles" refers to methodologies that can directly compute the vortical wake field of the rotor, based on the rotor-blade geometry and flowfield parameters. High-order spatially accurate methods are employed in conjunction with unsteady overset grid methodology to achieve a fully three-dimensional, unsteady, interactional simulation procedure. The benefits of employing high-order methods to capture wing/rotor-wake vortex structures have been well documented elsewhere.[16,17] In this effort a fifth-order scheme developed by Hariharan and Sankar[16,17] for the study of isolated rotors has been modified to address the rotor-airframe interaction problem.

A three-dimensional overset grid connectivity package for moving grids was also developed, based on the work in this area by Benek et al.[21] A generalized overset data structure in the connectivity allows for an arbitrary number of grids to interact with each other, with some hierarchical restrictions.[22] The high-order overset methodology is applied to simulate the Georgia Tech rotor-airframe model, for which abundant experimental data are available.[3–6] The vorticity structure in the flowfield, the mean, and unsteady surface-pressure distributions on the airframe are analyzed and compared to experimental data.

Received 26 March 2001; revision received 20 April 2003; accepted for publication 25 April 2003.

*Senior Engineer, Components Department.

†Regents Professor, School of Aerospace Engineering.

Mathematical Formulation

The three-dimensional unsteady, compressible Reynolds-averaged Navier–Stokes equations can be written in the generalized coordinate system as

$$\boldsymbol{q}_\tau + \widehat{\boldsymbol{F}}_\xi + \widehat{\boldsymbol{G}}_\eta + \widehat{\boldsymbol{H}}_\zeta = \widehat{\boldsymbol{F}}_{v_\xi} + \widehat{\boldsymbol{G}}_{v_\eta} + \widehat{\boldsymbol{H}}_{v_\zeta} \tag{1}$$

This equation is discretized as

$$\frac{3\boldsymbol{q}^{n+1,m} - 4\boldsymbol{q}^{n} + \boldsymbol{q}^{n-1}}{2\Delta\tau} + \frac{\bar{F}^{n+1,m}_{i+1/2} - \bar{F}^{n+1,m}_{i-1/2}}{\Delta\xi} + \frac{\bar{G}^{n,m-1}_{j+1/2} - \bar{G}^{n,m-1}_{j-1/2}}{\Delta\eta}$$
$$+ \frac{\bar{G}^{n,m-1}_{j+1/2} - \bar{G}^{n,m-1}_{j-1/2}}{\Delta\eta} + \frac{\bar{H}^{n+1,m}_{k+1/2} - \bar{H}^{n+1,m}_{k-1/2}}{\Delta\zeta} = \frac{\widehat{F}^{n,m}_{v_{i+1/2}} - \widehat{F}^{n,m}_{v_{i-1/2}}}{\Delta\xi}$$
$$+ \frac{\widehat{G}^{n,m-1}_{v_{j+1/2}} - \widehat{G}^{n,m-1}_{v_{j-1/2}}}{\Delta\eta} + \frac{\widehat{H}^{n,m}_{v_{k+1/2}} - \widehat{H}^{n,m}_{v_{k-1/2}}}{\Delta\xi} \tag{2}$$

Here $\bar{F}$ is the numerical flux that differs from the physical flux $\widehat{F}$ by a numerical viscosity term proposed by Roe.[23] $\bar{G}$ and $\bar{H}$ are numerical fluxes in the η and ζ directions, respectively. The details of the Roe scheme and its implementation are discussed in the next section. In Eq. (2) n is the time level, and m is a Newton subiteration counter. Equation (2) is linearized about the known iteration level $m - 1$, leading to a system of simultaneous linear equation for the quantity

$$\Delta q = q^{n+1,m} - q^{n+1,m-1} \tag{3}$$

This results in a system of equations, which results in a banded pentadiagonal block matrix

$$[A]\{\Delta q\} = \{R\}^{n+1,m-1} \tag{4}$$

where $\{R\}$ contains the most recent estimates for the flow properties for each of the terms shown in Eq. (2). The matrix $[A]$ can be inverted in a number of different ways. In the present work a diagonalized, approximate factorization scheme originally proposed by Pulliam and Chaussee[24] was used.

Roe Scheme for the Convective Fluxes

In this work the Roe scheme[23] was employed to compute the convective fluxes. In this scheme the convective fluxes are viewed as quantities transported by five distinct wave phenomena: two acoustic waves, one entropy wave, and two vorticity waves. The built-in viscosity of the vorticity waves is proportional to the local fluid velocity (along the direction of wave propagation) v_n. This component is thus diffused to a smaller extent in Roe scheme, compared to central difference schemes with added diffusion where all of the waves are diffused by an amount proportional to v_{n+a} (a is the speed of sound). In low subsonic regions v_{n+a} can be about five to ten times larger than v_n. Thus, conventional schemes diffuse vorticity more than the Roe scheme. This has been observed by other researchers (e.g., Simpson and Whitfield[25]), who found that classical boundary-layer problems can be captured by the Roe scheme with half of the number of points required by conventional schemes. The conventional implementations of Roe's scheme compute the flux crossing a cell face as follows (Fig. 1):

1) First, estimates of the flow properties to the left and right side of the face, q_L and q_R respectively, are computed.

2) Then, the flux is evaluated as

$$\bar{F} = \{[\boldsymbol{F}_1(\boldsymbol{q}_L) + \boldsymbol{F}_1(\boldsymbol{q}_R)]/2\} - |A|(\boldsymbol{q}_R - \boldsymbol{q}_L) \tag{5}$$

where

$$\boldsymbol{F}_1 = (\boldsymbol{F}\hat{\imath} + \boldsymbol{G}\hat{\jmath} + \boldsymbol{H}\hat{k}) . n\Delta S$$

where n is a unit normal to the cell surface. $|A|$ is the matrix $|\partial \boldsymbol{F}_1/\partial \boldsymbol{q}$, computed using special averages of $\boldsymbol{q}_L$ and $\boldsymbol{q}_R$. The various implementations of the Roe scheme differ from each other in the way

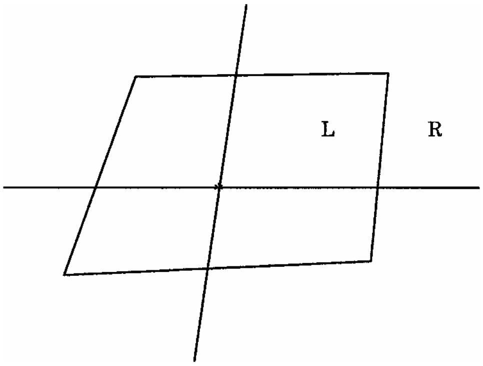

Fig. 1 Schematic of a finite volume cell around a grid point.

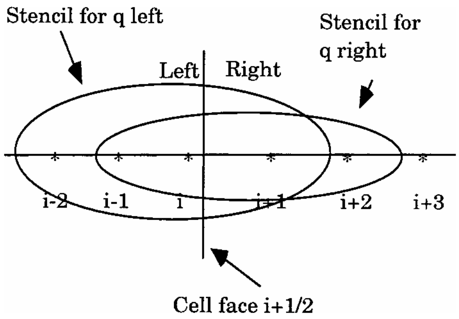

Fig. 2 Stencil used for the fifth-order scheme.

$\boldsymbol{q}_L$ and $\boldsymbol{q}_R$ are found at the cell face. For example, in a well-known third-order MUSCL[15] scheme

$$\boldsymbol{q}_L = \{1 + \Psi_i[(1 - \kappa)\nabla + (1 + \kappa)\Delta]/4\}\boldsymbol{q}_i$$
$$\boldsymbol{q}_R = \{1 - \Psi_{i+1}[(1 + \kappa)\nabla + (1 - \kappa)\Delta]/4\}\boldsymbol{q}_{i+1} \tag{6}$$

where $\kappa = \frac{1}{3}$, Δ/∇ are forward/backward difference operators, and Ψ_i is the adjustable parameter known as limiter. If limiters Ψ_i and Ψ_{i+1} are set to zero, a first-order-accurate solution will result. Most implementations define these parameters so that they automatically become zero near shock waves to avoid sampling across such shock waves.

The fifth-order scheme used in this work is based on the essentially nonoscillatory (ENO) scheme, developed by Harten et al.[26] The major steps in the ENO scheme are as follows:

1) Fifth-order polynomial fits for $\boldsymbol{q}_L$ and $\boldsymbol{q}_R$ are computed at face $(i + \frac{1}{2})$. The polynomial for $\boldsymbol{q}_L$ usually will involve nodes $(i - 2)$, $(i - 1)$, i, $(i + 1)$, $(i + 2)$, and the one for $\boldsymbol{q}_R$ will likewise usually involve $(i - 1)$, i, $(i + 1)$, $(i + 2)$, $(i + 3)$. Figure 2 shows the typical stencil used for the fifth-order fit. The coefficients of this polynomial must satisfy the following criteria.

a) At the nodes i, $i + 1$, etc., the average $\boldsymbol{q}$ value over the cell, obtained from the polynomial, must equal the node value $\boldsymbol{q}_i$, $\boldsymbol{q}_{i+1}$, etc.

b) If a polynomial using the nodes chosen is not "smooth," then a different set of node points are chosen to determine $\boldsymbol{q}_L$ and or q_R and, if necessary, drop the formal accuracy to a lower order.

2) The fluxes $\boldsymbol{F}_1$ and $\bar{F}$ are now computed as in the classical MUSCL scheme described earlier.

Overset Implementation

The idea behind the use of overset grids is to establish independent body-fitted grids around each of the components and solve the Euler/Navier–Stokes equations on these grids independently. The Georgia Tech rotor-body configuration consists of a two-bladed rotor in vicinity of a cylindrical body, as shown schematically in Fig. 3. For such a configuration three different grids are generated: two for the rotor blades and one for the cylindrical body. Figure 4a shows all three grids positioned appropriately in relation to one another.

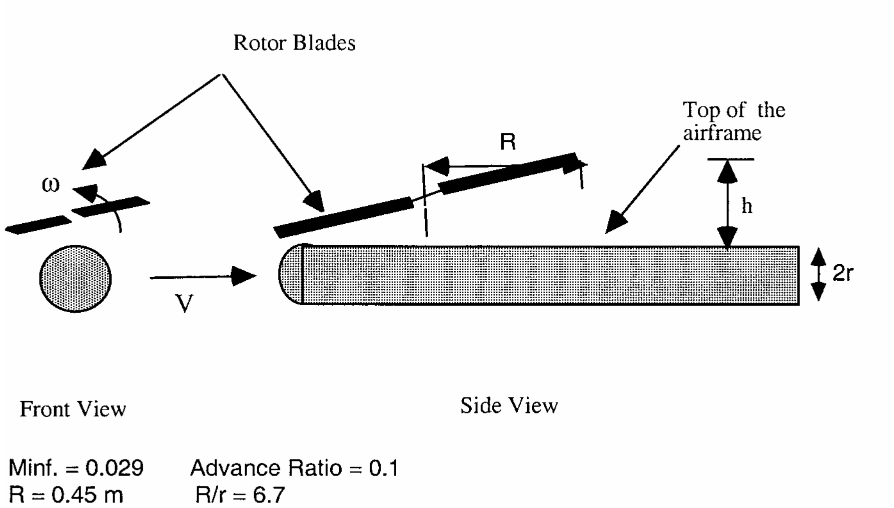

Fig. 3 Schematic of the Georgia Tech rotor-airframe configuration.

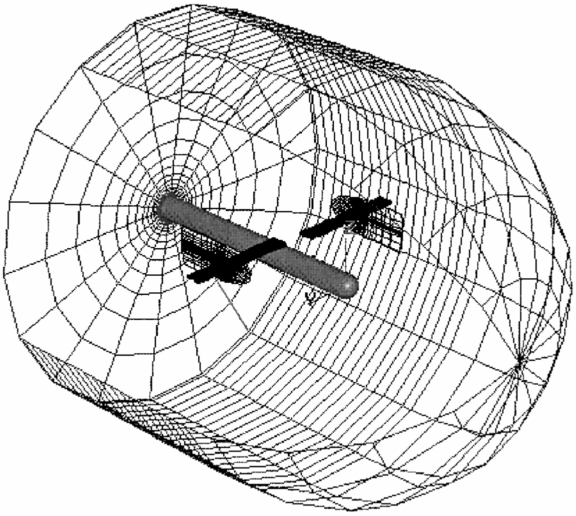

Fig. 4a Overset rotor-airframe grids used in the current simulation.

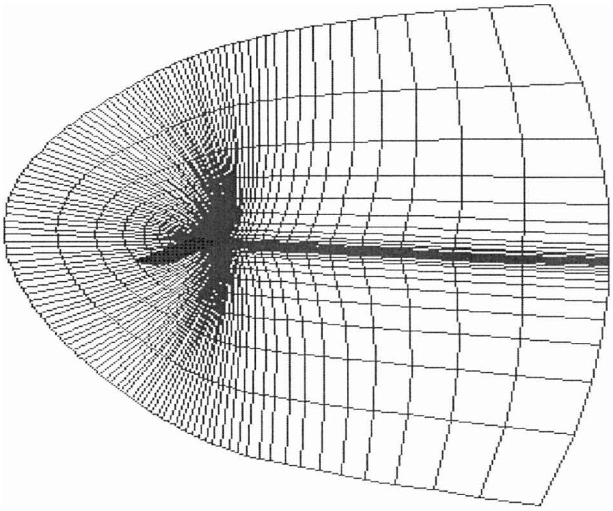

Fig. 4c C grids on one of the rotor blades.

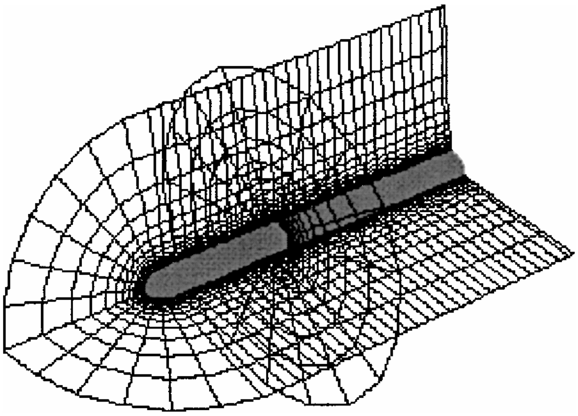

Fig. 4b O grid on the airframe.

Figures 4b and 4c show the body grid and the rotor-blade grids, respectively. Communication between these grids is then established through appropriate interpolations for the intergrid boundary points.

Central to an overset scheme is the information transfer between each of the grids that is required to advance the computational solution in each grid and is usually referred to as grid connectivity. Because the grids are overset in space, each of the grids acknowledges the overset presence of another grid by creation or modification of boundary points that derive information from the appropriate grid by interpolation. The oversetting process enforces some interior grid points in the major grids (i.e., the airframe grid in Fig. 4a) to be “blanked” out in order to create internal boundary points. Figure 5a shows a schematic illustrating the preceding process. For unsteady simulations in which the grids move relative to each other, such as the present effort, the grid-connectivity information has to be recomputed at every time step. Reference 22 gives a detailed discussion of the methodology, including an efficient means of achieving the necessary bookkeeping to track unsteady overset grid connectivity.

Once the grid-connectivity information is computed, the Navier–Stokes solver computes and updates the solution in all of the grid domains independently. The blanking produced by the overset grid connectivity needs to be recognized by the solver. The flux reconstruction should not access any information from the blanked grid points when computing fluxes in the vicinity of such points. The overset-boundary update routines use the information provided by the grid-connectivity package and the current flow solution provided by the solver to update the values at the overset boundary points of all of the grids involved in the simulation. The flowchart in Fig. 5b outlines the overset grid solution update process from a given time step to the next.

Grid Dynamics

The relative motion and spatial positioning of all of the grids involved in the simulation need to be updated at every time step.

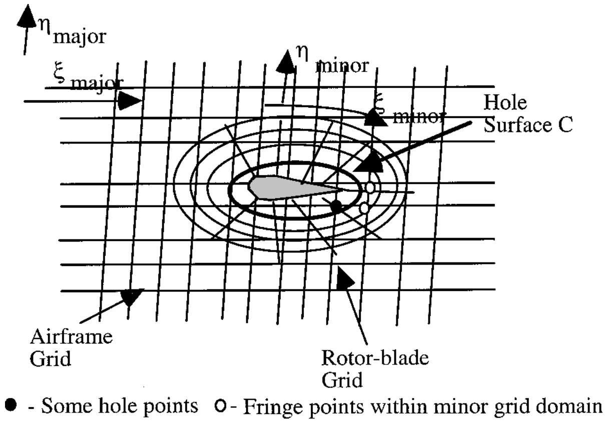

Fig. 5a Schematic illustrating hole/fringe points for overset grids.

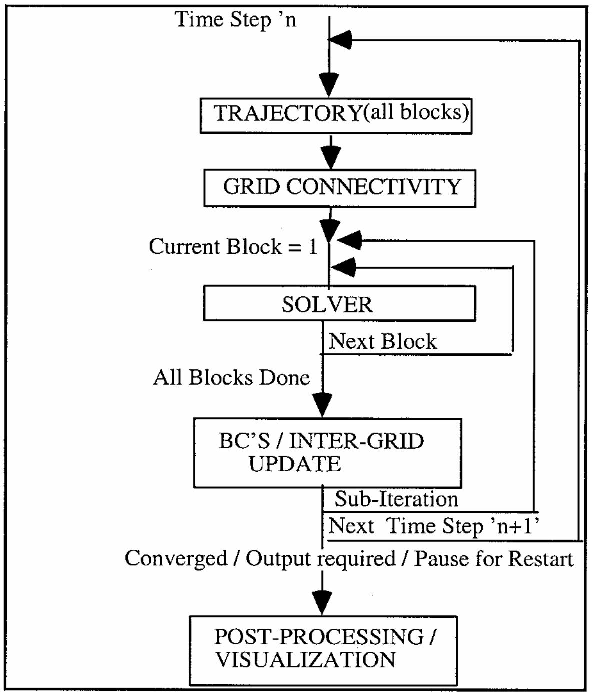

Fig. 5b Overall algorithm for the overset grid solution.

The grid motion could be prescribed or computed. For example, in the current rotor-airframe simulation the airframe moves with a forward flight Mach number of 0.2, and rotor revolves around a hub in the airframe with a tip Mach number of 0.44 with a prescribed tip path plane, flapping, cyclic pitch angles. On the other hand, aeroelastic deformations of the rotor blades can be computed from the evolving aerodynamic solution. In the current work the motion of the various grids involved is prescribed, and aeroelastic effects are ignored.

Generalized coordinate transformation matrices are computed to track the position of all of the grids involved in the simulation. Figure 6 shows the schematic of the orientation of the airframe and the rotor disk plane in global coordinates defined by unit vectors $\boldsymbol{i}, \boldsymbol{j}, \boldsymbol{k}$ in the x, y, and z directions, respectively. Figure 7 defines the local coordinate system for one of the rotor blades. The unit vectors $\boldsymbol{e}_x, \boldsymbol{e}_y, \boldsymbol{e}_z$ define a right-handed orthogonal coordinate system, fixed with the blade. Because the body-fitted C grid over the rotor blade is rigid in its motion, a single triad $\{\boldsymbol{e}_x, \boldsymbol{e}_y, \boldsymbol{e}_z\}$ can be defined for the entire grid. The transformation matrix $\boldsymbol{T}(n)$, between $\{\boldsymbol{e}_x, \boldsymbol{e}_y, \boldsymbol{e}_z\}$ and the Cartesian triad $\{\boldsymbol{i}, \boldsymbol{j}, \boldsymbol{k}\}$, needs to be established at all time steps.

$$\{\boldsymbol{e}_x, \boldsymbol{e}_y, \boldsymbol{e}_z\}^T = \boldsymbol{T}(n)\{\boldsymbol{i}, \boldsymbol{j}, \boldsymbol{k}\}^T \tag{7}$$

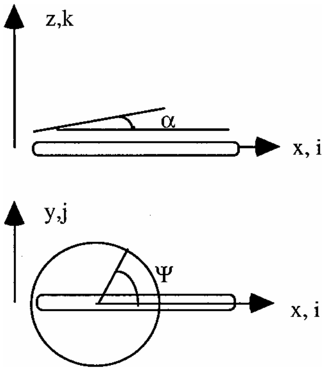

Fig. 6 Rotor-airframe orientation.

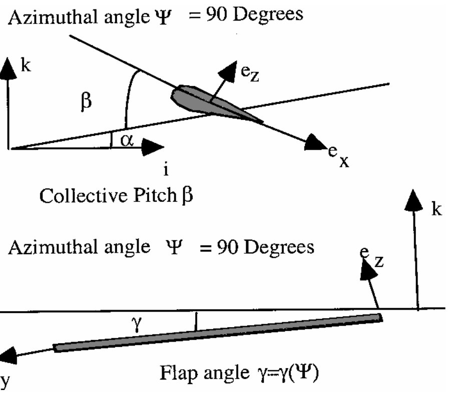

Fig. 7 Definition of the local blade coordinate system.

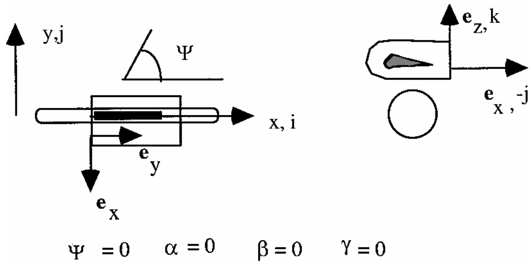

Fig. 8 Initial orientation of the rotor-blade grid as provided by grid generator.

In the preceding equation and all of the subsequent equations, $\{\}^T$ denotes the transpose of a vector or matrix. The rotor-blade grids were first generated independently and were supplied to the overset grid solver, with the blade aligned with the positive x axis as shown in Fig. 8.

The orientation of the rotor-blade grids at this instance can be defined by

$$\{\boldsymbol{e}_x, \boldsymbol{e}_y, \boldsymbol{e}_z\} = \{-\boldsymbol{j}, \boldsymbol{i}, \boldsymbol{k}\}$$

$$\begin{bmatrix} \boldsymbol{e}_x \\ \boldsymbol{e}_y \\ \boldsymbol{e}_z \end{bmatrix} = \begin{bmatrix} 0 & -1 & 0 \\ 1 & 0 & 0 \\ 0 & 0 & 1 \end{bmatrix} \begin{bmatrix} \boldsymbol{i} \\ \boldsymbol{j} \\ \boldsymbol{k} \end{bmatrix} \tag{8}$$

and hence the initial orientation matrix, which is defined as $\boldsymbol{M}_0 = \{\boldsymbol{e}_x, \boldsymbol{e}_y, \boldsymbol{e}_z\}^T$, can be written as

$$\boldsymbol{M}_0 = \begin{bmatrix} 0 & 1 & 0 \\ -1 & 0 & 0 \\ 0 & 0 & 1 \end{bmatrix} \tag{9}$$

This grid has to be moved such that the position of the grid at some given azimuthal angle Ψ corresponds to the prescribed rotor-blade position for that azimuthal angle Ψ. If the computations are started at $\Psi = 90$ deg ($\Psi = 270$ deg for the other blade), then the correct orientation of the grid can be achieved by the following set of transformations.

1) The grid is rotated by an angle $\alpha = \alpha_o$ about the local axis $\boldsymbol{e}_x$. This tilt of the rotor plane should be done at $\Psi = 0$. This can be represented as $[\boldsymbol{R}]_{e_x,\alpha_o}$. A generic rotation about a unit vector $\boldsymbol{n} = \{\boldsymbol{n}_x, \boldsymbol{n}_y, \boldsymbol{n}_z\}$ about some angle θ can be written as

$$[\boldsymbol{R}]_{n,\theta} = \begin{bmatrix} \boldsymbol{n}_x^2 + \cos(\theta)\left(1 - \boldsymbol{n}_x^2\right) \\ \boldsymbol{n}_x\boldsymbol{n}_y[1 - \cos(\theta)] + \boldsymbol{n}_z\sin(\theta) \\ \boldsymbol{n}_x\boldsymbol{n}_z[1 - \cos(\theta)] - \boldsymbol{n}_y\sin(\theta) \end{bmatrix} \times \begin{bmatrix} \boldsymbol{n}_x\boldsymbol{n}_y[1 - \cos(\theta)] - \boldsymbol{n}_z\sin(\theta) \\ \boldsymbol{n}_y^2 + \cos(\theta)\left(1 - \boldsymbol{n}_y^2\right) \\ \boldsymbol{n}_y\boldsymbol{n}_z[1 - \cos(\theta)] + \boldsymbol{n}_x\sin(\theta) \end{bmatrix} \times \begin{bmatrix} \boldsymbol{n}_x\boldsymbol{n}_z[1 - \cos(\theta)] + \boldsymbol{n}_y\sin(\theta) \\ \boldsymbol{n}_y\boldsymbol{n}_z[1 - \cos(\theta)] - \boldsymbol{n}_x\sin(\theta) \\ \boldsymbol{n}_z^2 + \cos(\theta)\left(1 - \boldsymbol{n}_z^2\right) \end{bmatrix} \tag{10}$$

Using preceding operator, the orientation matrix after this transformation can be written as

$$\boldsymbol{M}_1 = [\boldsymbol{R}]_{e_x,\alpha_o}\boldsymbol{M}_0 \tag{11}$$

2) The grid is rotated by an angle $\Psi = \Psi_o$ about the blade-fixed axis $\boldsymbol{e}_z$. The direction cosines of the blade-fixed axis e_z can be recovered from the orientation matrix $\boldsymbol{M}_1$. Performing this operation, the orientation matrix can be written as

$$\boldsymbol{M}_2 = [\boldsymbol{R}]_{e_z,\Psi_o}\boldsymbol{M}_1 \tag{12}$$

3) The grid is rotated by an angle $\beta = -\beta(\Psi_o)$, about the blade-fixed axis $\boldsymbol{e}_y$. The direction cosines of the blade-fixed axis e_y can be recovered from the orientation matrix $\boldsymbol{M}_2$. Performing this operation, the orientation matrix can be written as

$$\boldsymbol{M}_3 = [\boldsymbol{R}]_{e_y,-\beta}\boldsymbol{M}_2 \tag{13}$$

4) Finally, the grid is rotated by an angle $\gamma = \gamma(\Psi_o)$ about the blade-fixed axis $\boldsymbol{e}_x$. The direction cosines of the blade-fixed axis e_x can be recovered from the orientation matrix $\boldsymbol{M}_3$. Performing this operation, the orientation matrix can be written as

$$\boldsymbol{M}_4 = [\boldsymbol{R}]_{e_x,\gamma}\boldsymbol{M}_3 \tag{14}$$

The net transformation matrix for this rotor blade, excluding all translations, at time level $n = 0$ can be written as

$$\boldsymbol{T}(0) = \boldsymbol{M}_4^T \tag{15}$$

A similar transformation matrix can be written for the other rotor blade. Any grid point can be transformed from its original value in its prescribed orientation ($\boldsymbol{M}_0$) to the required orientation at the start of computation ($\boldsymbol{M}_4$, $t = 0$) by the transformation

$$\begin{bmatrix} x \\ y \\ z \end{bmatrix}_{t=0} = \boldsymbol{T}(0)\begin{bmatrix} x \\ y \\ z \end{bmatrix}_{\text{initial}} \tag{16}$$

The procedure would be complete if a way of computing the operator $\boldsymbol{T}(n)$ at a time level n can be prescribed, given the value of the operator $\boldsymbol{T}(n - 1)$ and position of all of the grid points $\{x, y, z\}$ at a previous time level $n - 1$. Assuming that the grid is oriented at the initial position, with orientation matrix $\boldsymbol{M}_0$, perform steps (1–4) with the appropriate values of all of the rotation angles, that is, $\Psi = \Psi(n)$, $\gamma = \gamma(\Psi)$, etc. This would result in the operator $\boldsymbol{T}(n)$, such that

$$\begin{bmatrix} x \\ y \\ z \end{bmatrix}_{t=n} = \boldsymbol{T}(\boldsymbol{n})\begin{bmatrix} x \\ y \\ z \end{bmatrix}_{\text{initial}} \tag{17}$$

The position vector $\{\boldsymbol{x}, \boldsymbol{y}, \boldsymbol{z}\}_{\text{initial}}$ can be obtained by

$$\begin{bmatrix} x \\ y \\ z \end{bmatrix}_{\text{initial}} = \boldsymbol{T}^{-1}(\boldsymbol{n} - 1)\begin{bmatrix} x \\ y \\ z \end{bmatrix}_{t=n-1} \tag{18}$$

Substituting for $\{\boldsymbol{x}, \boldsymbol{y}, \boldsymbol{z}\}_{\text{initial}}$ in Eq. (17) yields

$$\begin{bmatrix} x \\ y \\ z \end{bmatrix}_{t=n} = \boldsymbol{T}(\boldsymbol{n})\boldsymbol{T}^{-1}(\boldsymbol{n} - 1)\begin{bmatrix} x \\ y \\ z \end{bmatrix}_{t=n-1} \tag{19}$$

Equation (19) prescribes the net rotational transformation. By slightly modifying the representation of the position vector (using a four-dimensional representation $\{x, y, z, 1\}$), translations and shear (if any) can be also be included in one effective transformation matrix.

Overset Solver

The overset grid-connectivity computation produces invalid field points that need to be excluded out of the solution process. The required changes should be made when computing the residuals and when computing the implicit operators on the left-hand side of Eq. (4). These changes are discussed in this section.

The grid-connectivity routines supply an identifier array IBLANK with following setting, for all of the grids:

$$\begin{aligned} \text{IBLANK}(I, J, K) &= 0 \quad \text{if } (I, J, K) \text{ is a hole point or a fringe point} \\ &= 1 \text{ Otherwise} \end{aligned}$$

The implicit and the viscous operators are three-point central difference operators. Any such three-point stencil, centered around a grid point with IBLANK $= 1$, will always access only valid points, that is, no hole points will be accessed. Figure 9 compares a valid three-point stencil with an invalid three-point stencil. The stencil a) is centered about node i with IBLANK $= 1$, and it accesses only valid points, whereas stencil b), which is centered about a node with IBLANK $= 0$, accesses a hole point. Therefore, any computations done around valid field points will not be affected. However for higher-order stencils (say a five-point stencil), even a stencil centered on a valid field point can access a hole point as shown in Fig. 10.

Based on the preceding considerations, the diagonalized form of Eq. (4) can be written as follows:

$$[I + \Delta\tau\delta_\xi B \,.\, \text{IBLANK}_{\text{ijk}}] \,.\, [I + \Delta\tau\delta_\zeta C \,.\, \text{IBLANK}_{\text{ijk}}]\Delta q^{n+1} = R^n \,.\, \text{IBLANK}_{\text{ijk}} \tag{20}$$

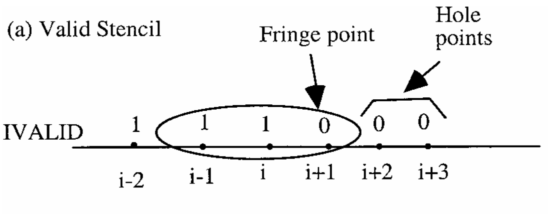
(a) Valid Stencil

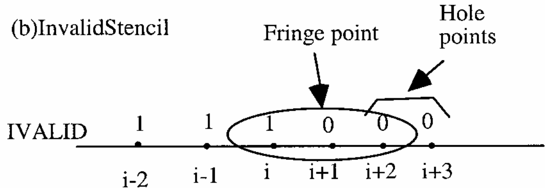
(b)InvalidStencil

Fig. 9 Schematics comparing of 1) Valid and 2) invalid three-point stencils.

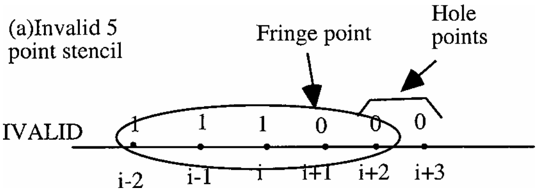

Fig. 10 Schematic of an invalid five-point stencil.

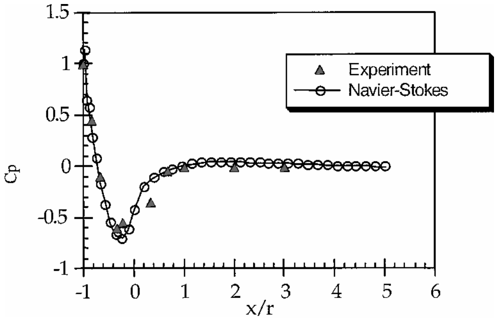

Fig. 11 Surface-pressure distribution along the crown line for the airframe without the rotor.

The residual R^n consists of the viscous and the inviscid contributions. The viscous residuals need no change, as a three-point operator is used to compute them. The computation of inviscid residuals needs modifications depending on the computational scheme used to compute the residual. For the third-order MUSCL scheme the projectors for the left and right fluxes in the ξ direction, as defined by Eq. (6), are modified as follows.

$$q_L = \{1 + \Psi_i[(1 - \kappa)\nabla + (1 + \kappa)\Delta]/4 \,.\, \mathrm{IBLANK}_{i-1} \,.\, \mathrm{IBLANK}_{i+2}\}q_i$$

$$q_R = \{1 - \Psi_{i+1}[(1 + \kappa)\nabla + (1 - \kappa)\Delta]/4 \,.\, \mathrm{IBLANK}_{i+1} \,.\, \mathrm{IBLANK}_{i-2}\}q_{i+1} \qquad (21)$$

Equation (21) ensures that the scheme reverts to first-order accuracy for both the left and the right projections in case a hole point is encountered in either the left or the right stencil.

For the fifth-order adaptive stencil ENO scheme, the stencil selection criterion is modified to reject any stencil that includes two adjacent hole points in it. This procedure allows the ENO scheme to automatically reject projections involving invalid hole points and still retain the fifth-order accuracy.

Results and Discussions

Configuration of Georgia Tech Rotor-Airframe Model

Figure 3 shows a schematic of the rotor-airframe model studied extensively at Georgia Tech. For this interaction between a rotor in lifting forward flight and a hemisphere-cylinder body, a large body of velocity field and surface-pressure data is available.[3–6] Relevant geometrical parameters and rotor-related parameters such as collective pitch, rotor tilt angle, and blade flapping angle are documented in Ref. 3. The rotor blades are rectangular planforms made up of NACA-0015 sections. For the case chosen the rotor and the airframe had a clearance of $h/R = 0.3$. The rotor had angular velocity of $\omega = 2100$ rpm, and the rotor-airframe system had an advance ratio of $\mu = 0.1$.

Prior to a full interactional modeling, a Navier–Stokes solution of the body in forward flight was obtained. An O grid was used, consisting of 71*31*31 points in the streamwise, azimuthal, and normal directions, respectively (Fig. 4b). Figure 11 shows the surface-pressure distribution over the isolated body without the rotor. Good agreement with the measured data is observed.

Fully Interactional Simulation

The dimensions of the airframe O grid were increased to 91*61*41 in the streamwise, azimuthal, and normal directions, respectively. An elliptic grid solver was used to further increase grid quality. Two C-H grids of dimensions 61*25*15 were generated independently over the rotor blades. The rotor grids were then oriented at their respective positions relative to the airframe grid. As time progressed, this relative position of the rotor grids with respect to the airframe grid was changed according to the actual rotor position at that time.

For the overset grid solution the three-step temporally second-order-accurate-scheme, with Newton iterations, was employed. The update of the solution in the boundary and the fringe points was delayed only by one sub iteration. The Newton iterations scheme, with implicit boundary conditions, allowed large time steps to be taken, reducing the number of calls to the overset grid-connectivity updates. A time-stepping equivalent to a rotor azimuthal advance of 0.12 deg per time step was achieved.

The solution on different grids could be obtained by different methodologies. For example, the solution over the body could be using a Navier–Stokes simulation and that over the rotor blades could be an Euler simulation. In this effort the Euler equations were solved on all of the grids to keep computational costs low.

Visualization of the Vorticity in the Flowfield

The tip vortex and vortex sheet generated by the two rotor blades descend towards the airframe. This convection is caused by a complex interaction between the self-induced motion of the vortex system and the freestream forward velocity. Visualizing the generation of the vortex and the subsequent tracking is vital to an understanding of the underlying physics of the interaction. Visualizing the vorticity is done with the aid of vorticity contours in chosen two-dimensional planes (usually one of the grid surfaces) and also with the use of vorticity isosurfaces.

Figure 12 illustrates the concepts involved in using overset grids. The vorticity contours are shown for the rotor grid in a streamwise plane behind the trailing edge of the rotor. Similar vorticity contours are shown for the airframe grid in an azimuthal plane along the crown line (the top of the airframe). The tip vortex and the vortex sheet are generated by the rotor blades in the C-grid zones. This system of vorticity is then transmitted over to the airframe grid by the grid-connectivity process. Once this vortex system is transmitted to the airframe grid, it convects down and impinges on the airframe.

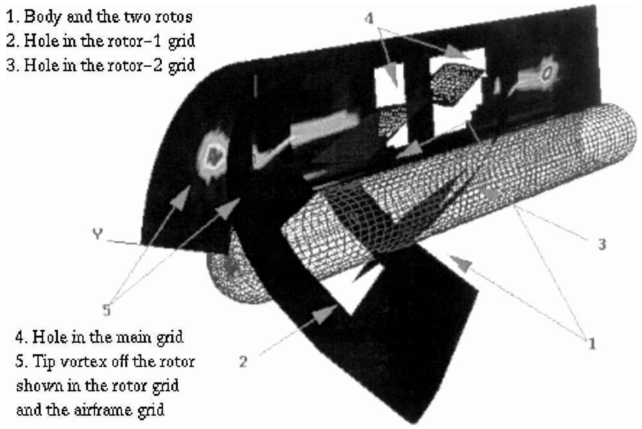

Fig. 12 Vorticity magnitude contours on the airframe and rotor grids.

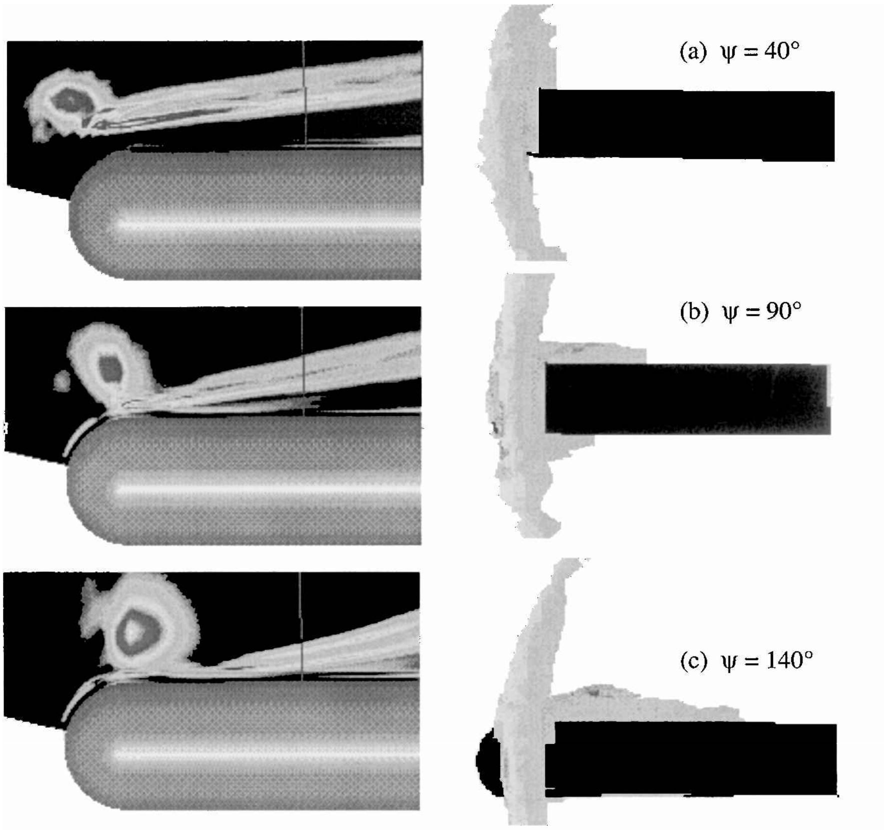

Vorticity contours on a normal plane along the crown line

Vorticity iso-surfaces (looking from top of the airframe)

Fig. 13 Impingement of the fore vortex on the surface of the airframe.

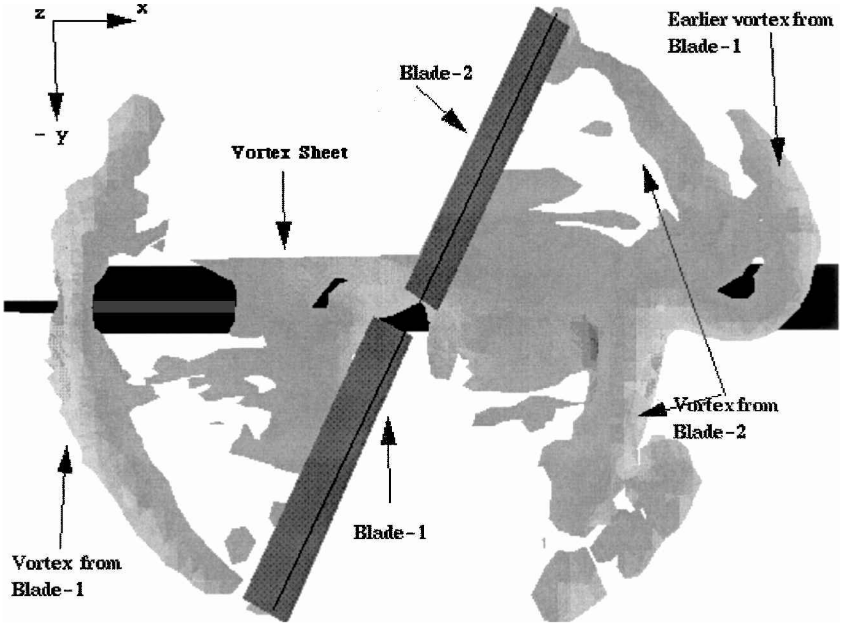

Fig. 14 Isovorticity surfaces in the flowfield. Vorticity surfaces colored from light to dark based on direction of normal velocity in the *z* direction.

Figure 12 also shows the various invalid holes that are generated at this instance.

Figure 13 shows three vorticity contour plots tracking the transmitted vortex in the airframe grid. The vorticity contours shown are on the azimuthal plane along the crown line on the left and as isosurfaces on right at three different vortex ages. The age of the vortex in terms of the azimuthal advance of the rotor, since the generation of the vortex, is indicated in the three contour plots. The first plot ($\Psi = 40$ deg) shows the position of the vortex, when the age of the vortex is 40 deg. In the subsequent plots ($\Psi = 90$ and 140 deg) this vortex moves down towards the airframe. The vortex eventually impinges, when the age of the vortex is approximately $\Psi = 220$ deg.

Figure 14 shows the isovorticity contours computed from the solution over the entire airframe grid at a given instance. The figure shows the position of the rotor blades, represented as blade-1 and blade-2, at that time level. In this figure the vortices coming off

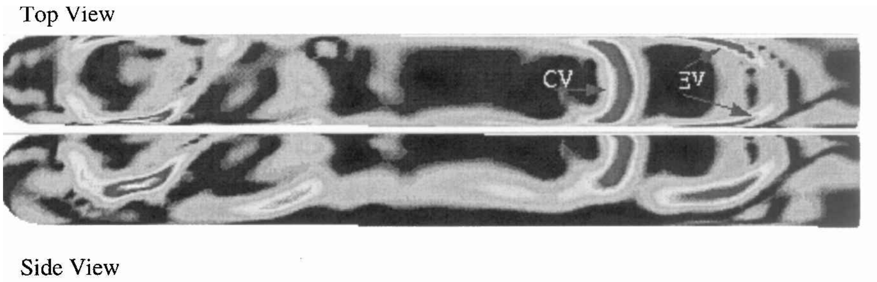

(a)Snap-1: Vortex Age – 200°

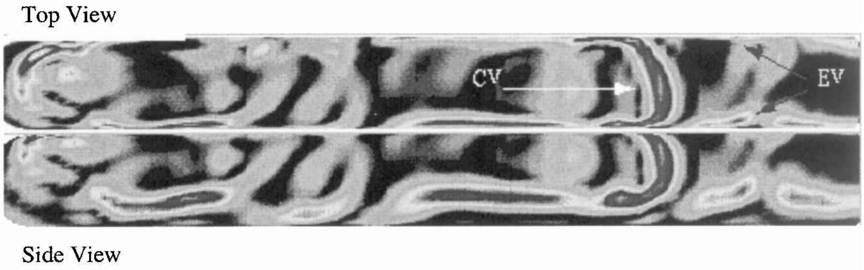

(b)Snap-2: Vortex Age – 259°

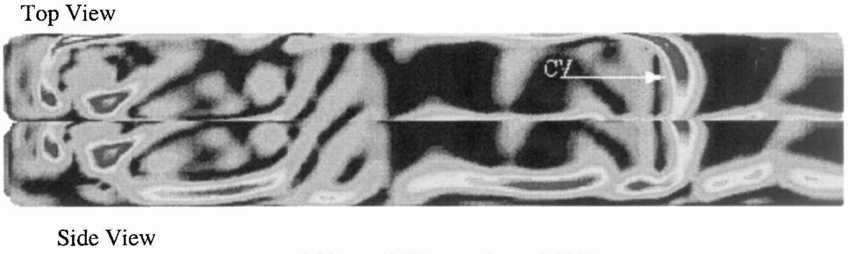

(c)Snap-3: Vortex Age - 320 Degrees

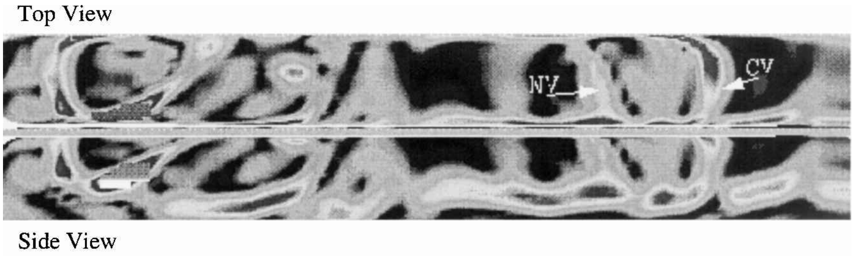

(d) Snap-4: Vortex Age – 356°

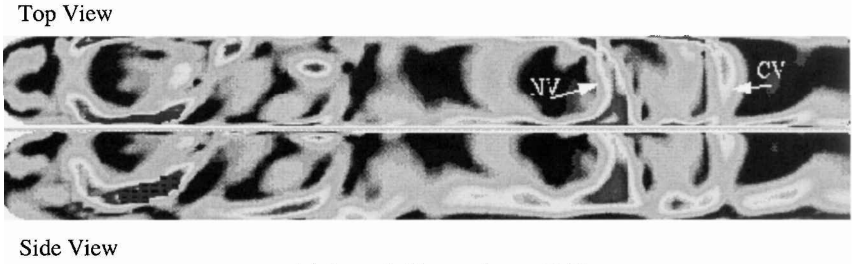

(e) Snap-5: Vortex Age – 381°

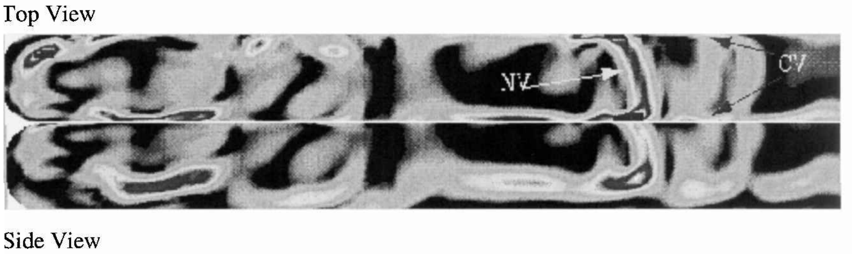

(f) Snap-6: Vortex Age – 405°

EV - Earlier Vortex **CV - Current Vortex** **NV - Next Vortex**

Fig. 15 Sequences of snapshots in time of vorticity contours in a normal plane just off the surface of the airframe. Each figure shows the top and side views.

Blade-1 and Blade-2 can be seen near the nose and aft of the airframe, respectively. Near the aft of the airframe, the earlier vortex that had been generated by Blade-1 as it passed over the aft of the airframe is also seen. This earlier vortex is about to hit the airframe. In the front portion only the most recent vortex (off Blade-1) is seen. The other earlier vortex (off Blade-2) is very close to the surface, at this instance, and has not been shown. The vortex isosurfaces seen near the center of the rotor are caused by the vortex sheet shed by both Blade-1 and Blade-2.

Figure 15 shows a sequence of vorticity plots that take a closer look at the vortex-surface interaction. These vorticity contours are plotted on a normal plane just off the surface of the airframe ($\Delta n = 0.05R$), that is, at a normal grid plane $\zeta = 3$ ($\zeta = 1$ is the airframe surface). Each of these snapshots in time shows the top and the side view of the interaction at that given instance. The age of the vortex, which is labeled as current vortex (CV), is provided for all of the pictures. In these figures the focus is on the aft vortex impingement. In Fig. 15a (vortex age = 200 deg), the current vortex and the remnants of an earlier vortex (EV) can be seen. In the subsequent pictures (Figs. 15b and c) the EV completes its interaction with the airframe, and the current convects down. In Fig. 15d (vortex age = 356 deg) the vortex generated most recently (NV) starts appearing in the region of interest, in the same position of that of the CV in Fig. 15a. Figures 15e (vortex age = 381 deg) and 15f (vortex age = 405 deg) complete the cycle, with the CV completing its interaction and the NV taking its position as the current vortex. This scenario repeats over and over again.

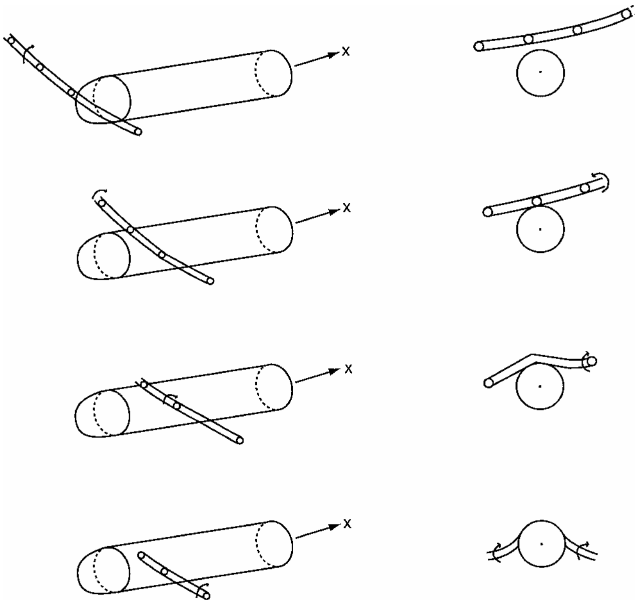

Fig. 16a Schematic of fore-vortex body interaction.

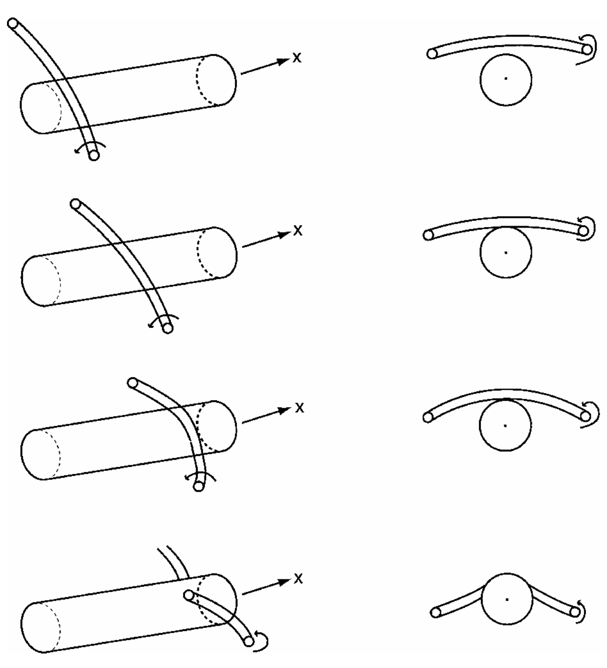

Fig. 16b Schematic of aft-vortex body interaction.

An interesting feature of the blade-vortex interaction with the airframe is the difference in the interactions between the fore and aft vortices with the airframe. Based on what is observed in Fig. 15, a sequence of schematics is drawn in Figs. 16a and 16b describing this interaction. In the sequence of images in Fig. 15, highlighted in schematic Fig. 16a, the fore vortex impinges sharply on the body and does not drag along the surface much. It is "cut" by the body quickly before it could traverse a greater length along the crown line of the airframe. The aft vortex, as seen on Fig. 15 and highlighted in schematic Fig. 16b, lingers along the crown line of the airframe before breaking up into two sections. The total number of vortices impinging on the fore and aft sections of the body remain the same. This implies that forebody vortices slow down in the freestream direction as it approaches the airframe, and the aftbody vortices speed up. This is fully consistent with classical vortex theory as illustrated in Fig. 17, which shows the image vortex and the net-induced velocities for the fore and aftbody vortices as they approach the airframe.

Mean Surface-Pressure Distribution

In the present analysis the rotor-blade geometric parameters (flapping, cyclic collective variation) are prescribed, and aeroelastic effects are ignored. But the wake structure and the interaction of the rotor-body system with the wake are computed. The mean and unsteady variation of the surface-pressure distribution are computed and compared with other analyses and experimental results. Figure 18 shows the comparison between the computed and measured mean surface pressures over the crown of the airframe. The mean pressure distribution is obtained by averaging the instantaneous pressures over a complete cycle of revolution of the rotor. The following key aspects can be noticed:

1) The aft C_p peak is captured well. The magnitude of the captured C_p peak near the nose (ahead of $x/R = 0.5$) is lower in magnitude compared to the experiments.

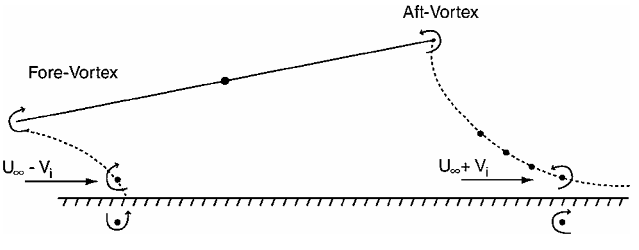

Fig. 17 Schematic of the image vortices and the resulting effect in the fore- and aft-vortex body interaction (V_i, induced velocity).

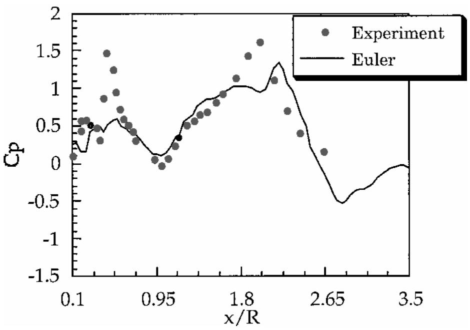

Fig. 18 Mean surface-pressure distribution along the crown line of the airframe.

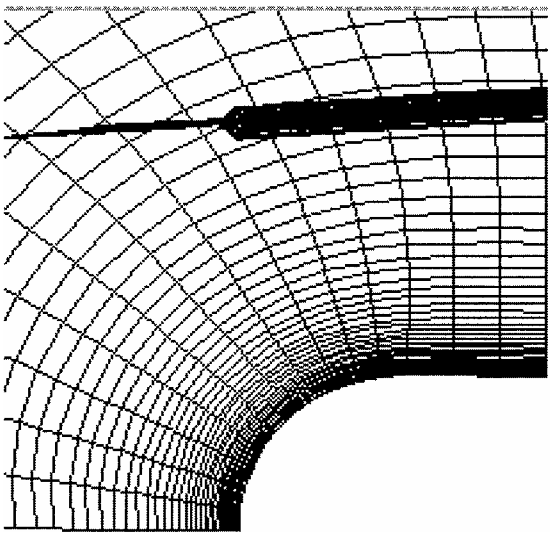

a) Relative position of the rotor blade

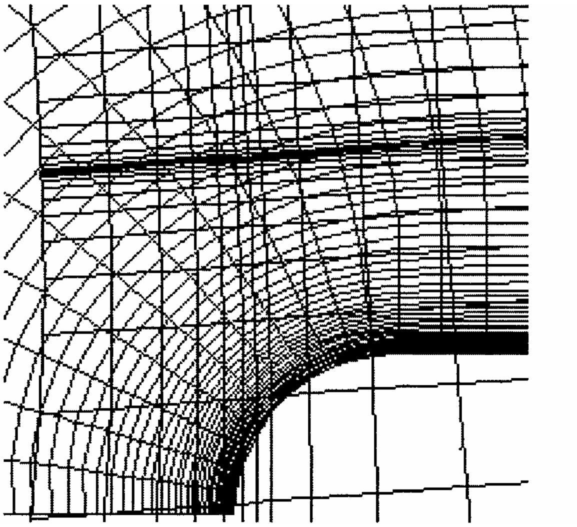

b) Airframe grid-Azimuthal plane. Rotor blade grid-Streamwise plane.

Fig. 19 Comparison of grid resolution between the rotor and airframe grids.

2) The front and aft C_p peaks seen in this figure are caused by the effects of blade passage. The streamwise location of the two blade passages induced increased C_p peaks is correctly predicted.

The C_p distribution ahead of $x/R = 0.5$ is not accurately predicted for a number of reasons. The rotor-airframe clearance is very small, that is, $h/R = 0.3$. Because the rotor is tilted forward, the clearance between the rotor and the airframe is small near the nose and large in the aft part of the airframe. The close proximity of the tip of the rotor and the nose of the airframe makes it difficult to match the grid resolutions of the airframe and rotor grids. This results in the diffusion of the tip vortex as it is transferred from the airframe to rotor grid. Figure 19 shows the resolution of the two grids near the nose of the airframe. Near the aft of the airframe, the rotor-airframe clearance is much larger, and the grids are better matched. The intergrid vortex transfer is relatively diffusion free, and therefore, the computed aft pressure peak compares more closely with the experimental values.

Figures 20 and 21 compare the mean pressure distribution along the crown line between the current simulation and earlier computations by Zori et al.[13] and Mavris.[11] The quality of the current first-principles-based simulation, in terms of capturing the mean surface-pressure distribution, is comparable to the solution obtained by Zori et al.[13] The solution obtained by Mavris[11] is seen to capture both the peaks better. The simulation of Mavris[11] directly derives information from experiments about the rotor wake, and the simulation by Zori et al.[11] depends on the experimental rotor-disk loading to compute the body forces that are to be input to the simulation. The current simulation methodology computes the wake information and with a better grid configuration can be used to study rotor-airframe configurations for which no experimental data are available.

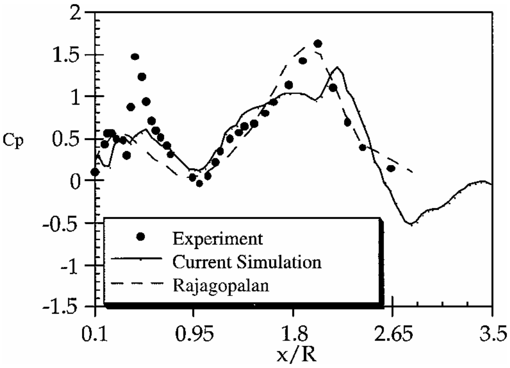

Fig. 20 Comparison of the mean surface-pressure distributions.

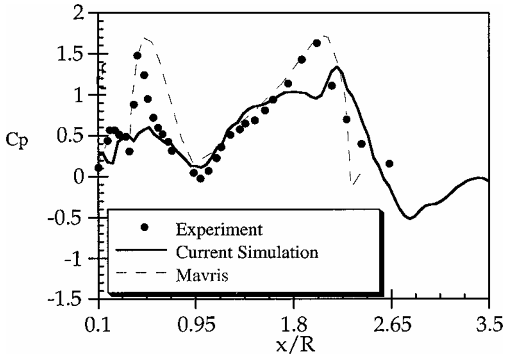

Fig. 21 Comparison of the mean surface-pressure distributions.

Instantaneous Surface-Pressure Distribution

Figure 22 illustrates the repeatability of the unsteady instantaneous pressure distribution along the crown line of the airframe. The comparison is for one rotor radius along the airframe, measured from the nose of the airframe. The figure shows the computed surface C_p values at a rotor azimuth position of $\Psi = 156$ deg, for two successive half-revolutions of the rotor.

Figures 23a–23e show the instantaneous pressure distribution along the crown line of the airframe, for a number of rotor azimuthal positions as the blade passes over the nose of the airframe (in the vicinity of $\Psi = 180$ deg). A smaller schematic in each of these figures indicates the relative position of the rotor and the airframe at that instance. As the rotor blade approaches the nose, the finer variations in pressure are caused by all of the previous tip vortices and vortex sheets. The effects of the residual vortex system are captured adequately, as seen in Figs. 23a ($\Psi = 144$ deg) and 23b ($\Psi = 156$ deg). The simulation also correctly predicted the blade passage increase in C_p when the rotor blade was advancing closer to the airframe. This is seen in Fig. 23c, when the rotor blade is at an azimuthal angle of $\Psi = 174$ deg. The blade-passage effect when the rotor blade is passing right above the airframe is shown in Fig. 23d. Once the blade passes over, the vortex generated by the blade passing over half a revolution earlier starts interacting with the airframe surface. Figure 23e shows the pressure distribution when rotor blade is at an azimuthal angle of $\Psi = 6$ deg. The pressure blip, caused by the vortex interacting with the airframe, is captured. The subsequent vortex interaction (i.e., $\Psi = 24, 48$, etc.) is not captured well.

One of the principal reasons for the variations in the degree of agreement of the computed instantaneous pressure distributions in

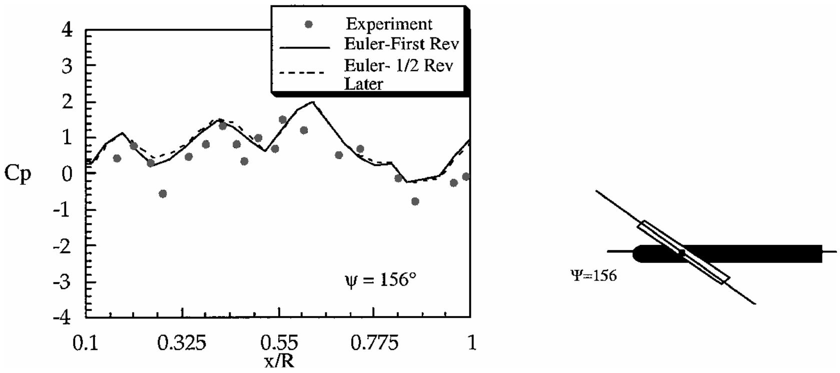

Fig. 22 Instantaneous surface-pressure distributions at two successive half-revolutions.

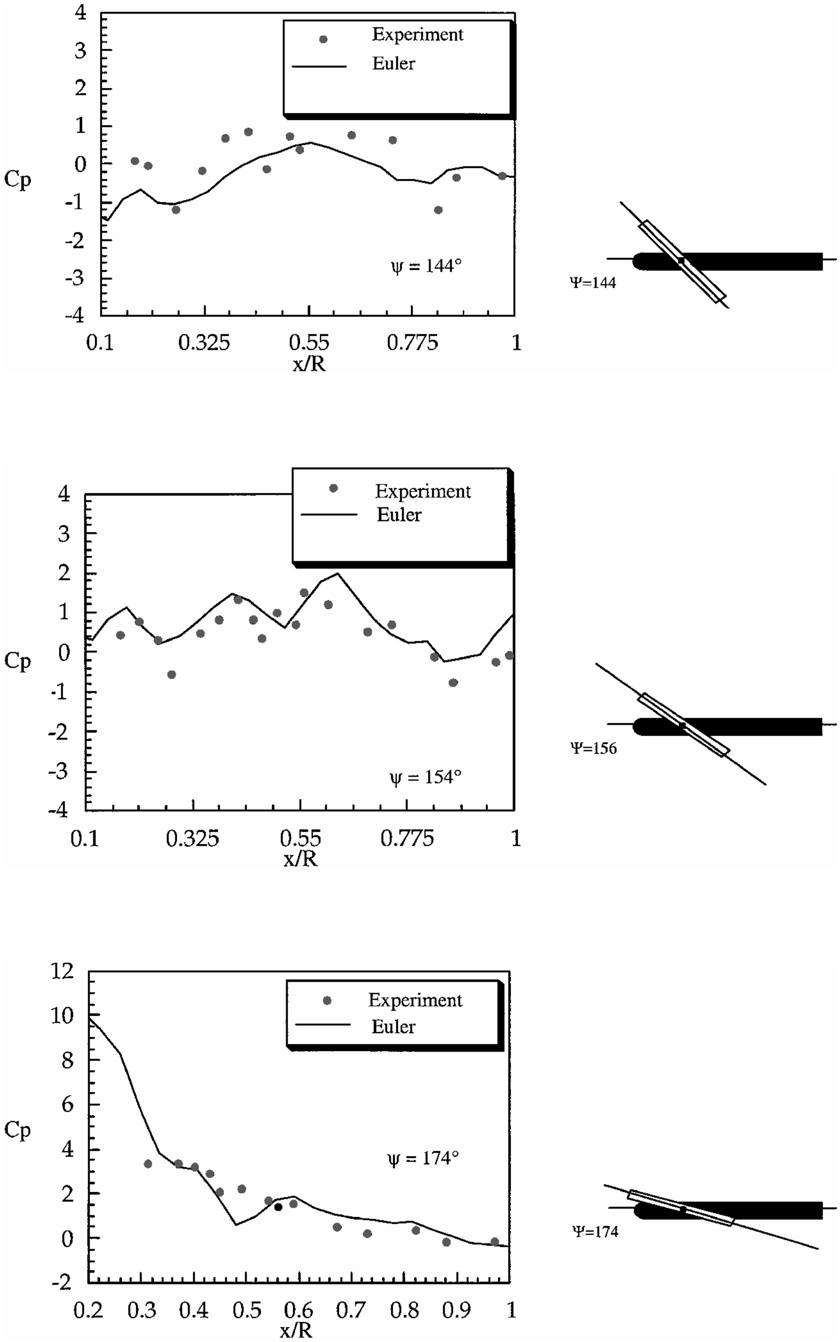

Fig. 23 Instantaneous surface-pressure distribution along the crown line of the airframe.

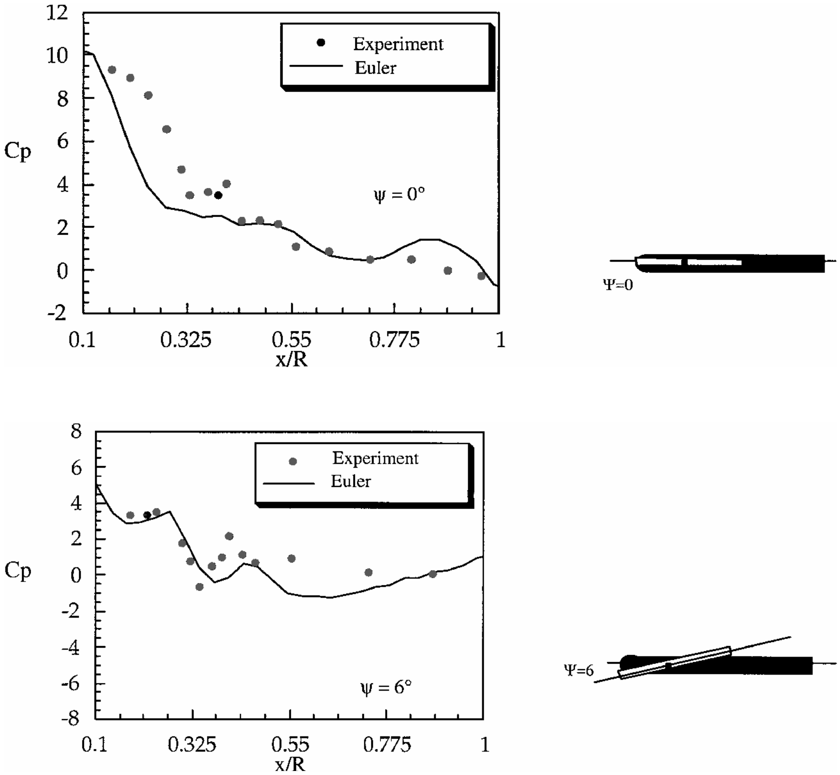

Fig. 23 Instantaneous surface-pressure distribution along the crown line of the airframe (continued).

comparison with experimental values is the diffusion of the wake-vortex structure across the overset grid boundaries. The weakening of the vortex system during the transfer between the two grids is attributable to the following reasons:

1) The intergrid interpolation process is only first-order accurate in space.

2) The grid resolutions of the airframe and blade grids need to be matched better in the vortex transfer region.

Conclusions

Fully interactional, three-dimensional unsteady flow simulation is done for a rotor-airframe aerodynamic interaction using a second-order temporally accurate, fifth-order spatially accurate, Euler/Navier–Stokes, overset-grid solver. This simulation does not require external aerodynamic inputs about the wake, such as the tip vortex strength and trajectory. Visualizing the vorticity pattern in the computed flowfield solutions and comparing the mean/instantaneous pressure distributions on the surface of the airframe obtained physical insights.

The current work incorporates two ingredients to solve a difficult problem, that is, 1) high-order methods and 2) overset grids. The fifth-order ENO scheme that had earlier demonstrated the ability to capture vorticity efficiently ensured that the blade vortex system did not diffuse excessively because of numerical dissipation. On a relatively coarse grid the high-order overset methodology captured the gross features of the flowfield with acceptable accuracy. However, the finer features such as instantaneous pressure distributions were captured only in certain instances of the rotor–blade location, indicating a need for further improvement/refinement of the grids involved in the simulation.

The use of overset grids makes it feasible to simulate rotor-airframe interactions, wherein rotor blades move relative to the airframe. If nonoverset grids were used (i.e., unstructured, etc.), the computational zone has to be regridded every so often and would present a cumbersome problem. However, overset grids do present their own set of problems. The use of overset grids shifts the difficulty of regridding when using single zone or unstructured grid approaches to the difficulty of maintaining grid resolution match between the rotor-blade grids and the airframe grids. Such problems can be tackled by using uniform intermediate meshes and increased number of grid points. Further research is also necessary to minimize the loss of accuracy in computation in the interfaces between the various overset grids.

Acknowledgment

This work was supported by the ARO CERT Contract DAAL 03-93-G-0002. Tom Doligalski was the project monitor.

References

[1] Sheridan, P. F., and Smith, R. P., "Interactional Aerodynamics—A New Challenge to Helicopter Technology," *Journal of the American Helicopter Society*, Vol. 25, No. 1, 1980, pp. 3–21.

[2] Smith, C. A., and Betzina, M. D., "Aerodynamic Loads Induced by a Rotor on a Body of Revolution," *Journal of the American Helicopter Society*, Vol. 31, No. 1, 1986, pp. 29–36.

[3] Brand, A. G., Komerath, N. M., and McMahon, H. M., "Surface Pressure Measurement on a Body Subject to Vortex Wake Interaction," *AIAA Journal*, Vol. 27, No. 5, 1989, pp. 569–574.

[4] Liou, S. G., Komerath, N. M., and McMahon, H. M., "Measurement of the Interaction Between a Rotor Tip Vortex and a Cylinder," *AIAA Journal*, Vol. 28, No. 6, 1990, pp. 975–981.

[5] Brand, A. G., "An Experimental Investigation of the Interaction Between a Model Rotor and Airframe in Forward Flight," Ph.D. Dissertation, School of Aerospace Engineering, Georgia Inst. of Technology, Atlanta, May 1989.

[6] Liou, S. G., "Velocity Measurements on a Lifting Rotor/Airframe Configuration in Low Speed Forward Flight," Ph.D. Dissertation, School of Aerospace Engineering, Georgia Inst. of Technology, Atlanta, Dec. 1988.

[7] Kim, J., "An Experimental Study of the Interaction Between a Rotor Wake and an Airframe with and Without Flow Separation," Ph.D. Dissertation, School of Aerospace Engineering, Georgia Inst. of Technology, Atlanta, May 1993.

[8] Crouse, G. L., Leishman, J. G., and Bi, N., "Theoretical and Experimental Study of Unsteady Rotor/Body Aerodynamic Interactions," *Proceedings of the 46th Annual Forum of the American Helicopter Society*, American Helicopter Society, Alexandria, VA, Vol. 2, May 1990, pp. 1075–1087.

[9] Berry, J. D., and Althoff, S. L., "Inflow Velocity Perturbations due to Fuselage Effects in the Presence of a Fully Interactive Wake," *Proceedings of the 46th Annual Forum of the American Helicopter Society*, Vol. 2, American Helicopter Society, Alexandria, VA, May 1990, pp. 1111–1120.

[10] Clark, D. R., and Maskew, B., "A Re-Examination of the Aerodynamics of Hovering Rotors Including the Presence of the Fuselage," *Proceedings of the 47th Annual Forum of the American Helicopter Society*, American Helicopter Society, Alexandria, VA, Vol. 2, May 1991, pp. 1–12.

[11] Mavris, D. N., "An Analytical Method for the Prediction of Unsteady Rotor/Airframe Interactions in Forward Flight," Ph.D. Dissertation, School of Aerospace Engineering, Georgia Inst. of Technology, Atlanta, Nov. 1988.

[12] Lorber, P. F., and Egolf, T. A., "An Unsteady Helicopter Rotor-Fuselage Aerodynamic Interaction Analysis," *Journal of the American Helicopter Society*, Vol. 35, No. 3, 1990, pp. 32–42.

[13] Zori, L. A. J., Mathur, S. A., and Rajagopalan, R. G., "Three-Dimensional Calculations of Rotor-Airframe Interaction in Forward Flight," American Helicopter Society, Paper 1992-0603, June 1992.

[14] Chaffin, M. S., and Berry, J. D., "Navier–Stokes and Potential Theory Solutions for a Helicopter Fuselage and Comparison with Experiment," ATCOM TR-94-A-013, NASA Langley Research Center, VA, June 1994.

[15] Srinivasan, G. R., and Baeder, J. D., "TURNS: A Free-Wake Euler/Navier–Stokes Numerical Method for Helicopter Rotors," *AIAA Journal*, Vol. 31, No. 5, 1993, pp. 959–962.

[16] Hariharan, N., and Sankar, L. N., "Higher Order Numerical Simulation of Rotor Flow Field," American Helicopter Society, Paper 1994-0511, May 1994.

[17] Hariharan, N., and Sankar, L. N., "Application of ENO Schemes to Rotary Wing Problems," AIAA Paper 95-1892, June 1995.

[18] Duque, E. P. N., and Dimanlig, A. C. B., "Navier–Stokes Simulation of the AH-66 (Comanche) Helicopter," *Proceedings of American Helicopter Society Aeromechanics Specialists Conference for Aerodynamics, Acoustics, and Dynamics*, American Helicopter Society, San Francisco, CA, Jan. 1994, pp. 3.7-1–3.7-15.

[19] Meakin, R. L., "Moving Body Overset Grid Methods for Complete Aircraft Tiltrotor Simulations," AIAA Paper 93-3350, July 1993.

[20] Ahmad, J., and Duque, E. P. N., "Helicopter Rotor Blade Computation in Unsteady Flows Using Moving Embedded Grids," AIAA Paper 94-1922, June 1994.

[21] Benek, J. A., Buning, P. G., and Steger, J. L., "A 3-D Chimera Grid Embedding Technique," AIAA Paper 85-1523, July 1985.

[22] Hariharan, N., "High Order Simulation of Unsteady Compressible Flows over Interacting Bodies with Overset Grids," Ph.D. Dissertation, School of Aerospace Engineering, Georgia Inst. of Technology, Atlanta, Sept. 1995.

[23] Roe, P. L., "Approximate Riemann Solvers, Parameter Vectors, and Difference Schemes," *Journal of Computational Physics*, Vol. 43, Oct. 1981, pp. 357–372.

[24] Pulliam, T. H., and Chaussee, D. S., "A Diagonal Form of an Implicit Approximate-Factorization Algorithm," *Journal of Computational Physics*, Vol. 39, Feb. 1981, pp. 347–363.

[25] Simpson, L. B., and Whitfield, D. L., "A Flux-Difference Split Algorithm for Unsteady Thin-Layer Navier–Stokes Solutions," *AIAA Journal*, Vol. 30, No. 4, 1992, pp. 914–922.

[26] Harten, A., Enquist, B., Osher, S., and Chakravarthy, C. R., "Uniformly High Order Accurate Essentially Non-Oscillatory Schemes," *Journal of Computational Physics*, Vol. 71, No. 2, April 1987, pp. 231–303.